Electronic Supplementary Material (ESI) for Nanoscale.

Supporting Information

Auto-Generated Iron Chalcogenide Microcapsules Ensured High-Rate and High-Capacity Sodium-Ion Storage

Xusheng Wang,[a,b] Zhanhai Yang,[a] Chao Wang,[b] Luxiang Ma,[b] Chunsong Zhao,[b] Jitao Chen,[b] Xinxiang Zhang[b] and Mianqi Xue*[a]

[a]Institute of Physics and Beijing National Laboratory for Condensed Matter Physics, Chinese Academy of Sciences, Beijing 100190, China.

[b]Beijing National Laboratory for Molecular Sciences College of Chemistry and Molecular Engineering, Peking University, Beijing 100871, China.

Email: xuemq@iphy.ac.cn

EXPERIMENTAL SECTION

Reaction Between the Iron Wires and Selenium/Tellurium Powders. The iron wires (0.25 mm in diameter and 25 mm in length) were polished before use. Then the iron wires and selenium/tellurium powders were placed at each end of a quartz tube, which was then sealed in the vacuum condition and heated at 500 °C for 150 h to obtain the reaction products.

Synthesis of the FeSe@FeS, FeS, FeSe, $Na_3V_2(PO_4)_3$ (NVP), $LiCoO_2$, and NCA Materials. The iron (Alfa Aesar, 99.9%), sulfur (Alfa Aesar, 99.5%), and selenium (Alfa Aesar, 99.999%) powders were mixed uniformly in a mortar at the molar ratio of 1: 0.75 : 0.25. The mixture was transferred into a quartz tube, which was then sealed in the vacuum condition and heated at 400 °C for 50 h to obtain the FeSe@FeS material. The FeS and FeSe materials were synthesized with the same procedure as comparison. The NVP material was synthesized by using a sol-gel method with NaOH, NH_4VO_3, $NH_4H_2PO_4$, and citric acid as raw materials. The $LiCoO_2$ and NCA (lithium nickel cobalt aluminum oxide) materials were synthesized by the conventional high-temperature solid-state reaction.

Synthesis of the Intermediate A, Intermediate B, Fe@FeS, and FeSe/FeS Materials. The intermediates A and B were selected from the synthesis process in Fig. S5 and taken out of the muffle furnace and cooled to room temperature in a very short time. The Fe@FeS material was prepared with the iron and sulfur powders at a molar ratio of 1 : 0.75 by using the synthesis process in Fig. S5. The FeSe/FeS material was prepared with the Fe@FeS material and Se powders at a molar ratio of 1 (Fe): 0.25 (Se) by using the synthesis process in Fig. S5.

Material Characterizations. The crystal structures of FeSe@FeS, Fe@FeS, and FeSe/FeS materials were determined by X-ray diffraction (XRD, PANalytical diffractometer) with Cu Kα

radiation (λ = 1.5416 Å) (40 kV, 40 mA). The morphological, elemental-mapping, and microstructural characterizations of FeSe@FeS, FeS, Fe@FeS, and FeSe/FeS materials were visualized by scaning electron microscopy (SEM, S4800, Hitachi) and transmission electron microscopy (TEM, JEM-2100F, JEOL). The thermal stability of the FeSe@FeS material was evaluated by differential scanning calorimetry (DSC, Q100DSC, TA) (DCS1 of METTLER TOLEDO for the $LiCoO_2$ and NCA materials).

Preparation of the FeSe@FeS, FeS, FeSe, NVP, $LiCoO_2$, and NCA Electrodes. The low mass-loaded FeSe@FeS electrodes were prepared by mixing the FeSe@FeS powders, carbon black, and sodium carboxymethylcellulose (CMC) at a weight ratio of 8 : 1 : 1. The slurry was spread on a copper foil and then dried in an electric thermostatic drying oven at 90 °C. The dried copper foil was cut into disks (11 mm) as the FeSe@FeS electrodes and then dried in an oven at 80 °C for 12 h under vacuum (the loading is 1.6 mg cm^{-2}). The FeS and FeSe electrodes were prepared by the same procedure for comparison. The high mass-loaded FeSe@FeS electrodes were prepared by the similar procedure only with the differences of LA133 binder (acrylonitrile copolymer dispersed in water) as the binder and the weight ratio of 85 : 8 : 7. The NVP electrodes were prepared by mixing the NVP powders (90 wt% of pure NVP and 10 wt% of carbon), carbon black, and polyvinylidene fluoride (PVDF) at a weight ratio of 75 : 15 : 10. The slurry was spread on the aluminum foils and then dried in an electric thermostatic drying oven at 90 °C. The dried aluminum foils were cut into disks (11 mm) as the NVP electrodes and then dried in an oven at 120 °C for 12 h under vacuum. The $LiCoO_2$, and NCA electrodes were prepared by the similar procedure only with the difference of the weight ratio of 90 : 5 : 5.

Electrochemical and Battery Performances of the FeSe@FeS, FeS, FeSe, NVP, $LiCoO_2$, and NCA Electrodes. The electrochemical and half-cell performances of FeSe@FeS, FeS, and

FeSe electrodes were characterized with sodium metal foils as the counter electrodes, glass fibers as the separators, and 1 mol L^{-1} sodium trifluomethanesulfonate ($NaCF_3SO_3$) in diethylene glycol dimethyl ether (DEGDME) as the electrolyte, and then assembled into LIR2032-type coin cells in an argon-filled glove box in which the moisture and oxygen contents were below 0.1 ppm. The half-cell performances of the NVP electrodes were characterized by the similar procedure only with the differences of the sodium metal foils as the anode and 1 mol L^{-1} sodium perchlorate ($NaClO_4$) in propylene carbonate (PC) with 5 vol% fluoroethylene carbonate (FEC) as the electrolyte. The full-cell performances of the FeSe@FeS electrodes were characterized by the similar procedure only with the differences of the NVP as the cathode and 1 mol L^{-1} $NaClO_4$ in DEGDME as the electrolyte. The $LiCoO_2$ and NCA electrodes were assembled in the same procedure only with the differences of lithium metal foils as the counter electrodes, Celgard 2400 as the separators, and 1 mol L^{-1} lithium hexafluorophosphate ($LiPF_6$) in a mixture of ethylene carbonate (EC), dimethyl carbonate (DMC), and ethyl methyl carbonate (EMC) (v : v : v = 1 : 1 : 1) as the electrolyte. The cycling and rate tests of the assembled batteries were performed on a Land CT2001A battery testing system within the voltage range of 0.25-3.0 V *versus* Na^+/Na (0.01-3.0 V in the Fig. S19c; 2.2-4.0 V for the NVP half cells, and 0.3-2.9 V for the full cells). Cyclic voltammogram (CV) (0.25-3.0 V) and electrochemical impedance spectroscopy (EIS) were measured on an Autolab electrochemical workstation. The cycle number of the cycling performances for the FeSe@FeS half cells in the text starts after several discharge-charge processes, in which a small current density (100-500 mA g^{-1}) was used to activate the electrodes to achieve the stable cycling state.

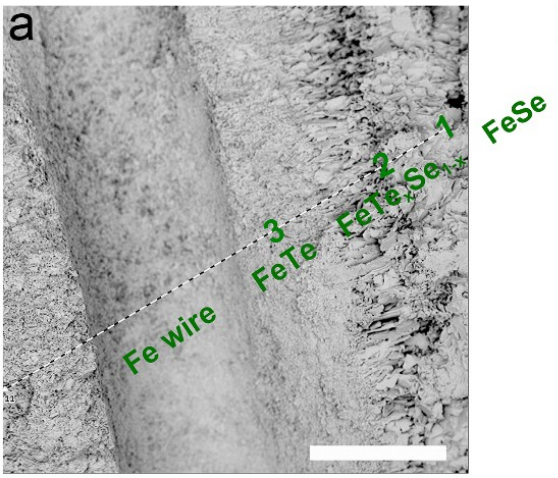

b

Site / Element	1	2	3
Selenium	17.2	5.9	0.0
Tellurium	25.0	34.1	48.9

Fig. S1 (a) SEM image of the reaction products between the iron wires and selenium/tellurium powders. It shows a hierarchical structure: inner FeTe, middle $FeSe_xTe_{1-x}$, and outer FeSe (with gradually reduced Te component). (b) EDX results of the atomic percents of selenium and tellurium at the sites of 1, 2, and 3 in panel (a). The scale bar is 200 μm in panel (a).

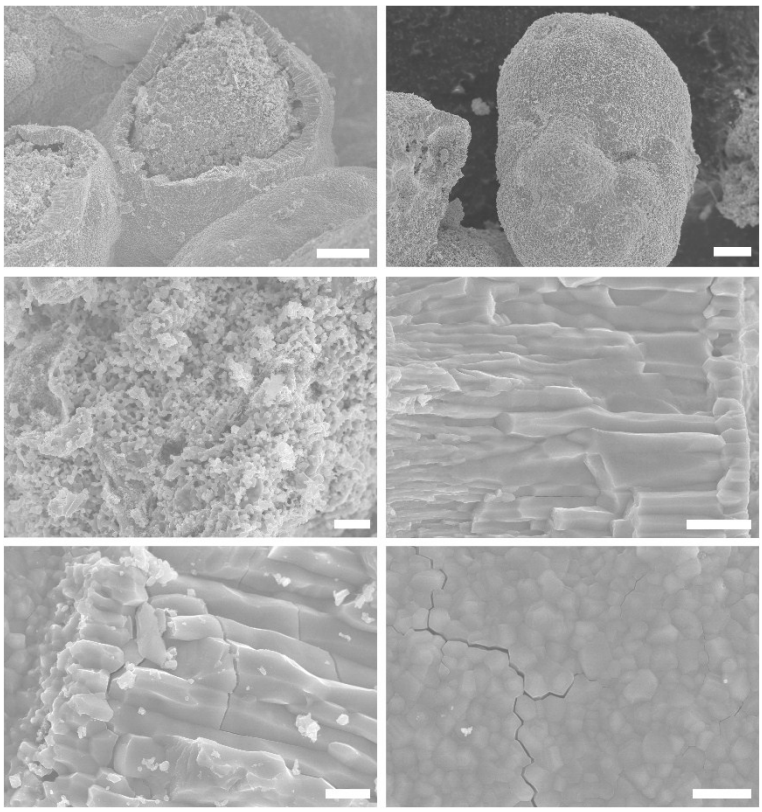

Fig. S2 (a-d) SEM images of the FeSe@FeS material. (e-f) SEM images of the contrastive FeS material. The morphology of FeS is very similar to that of the shell-encapsulation structure of the FeSe@FeS material. The scale bars are severally 20, 10, 2, 2, 1, and 1 μm in panels (a-f).

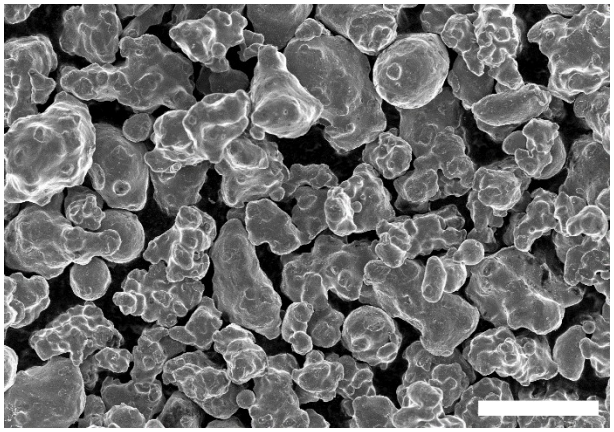

Fig. S3 SEM image of the raw iron powders. The scale bar is 50 μm.

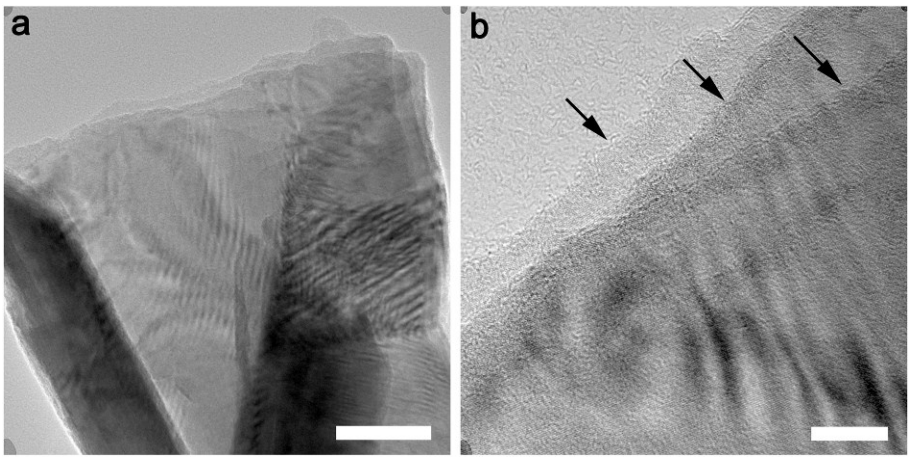

Fig. S4 TEM images of the FeSe@FeS material. The layered configuration extends energetically along the planar dimensionality. The scale bars in panels (a) and (b) are 50 and 10 nm, respectively.

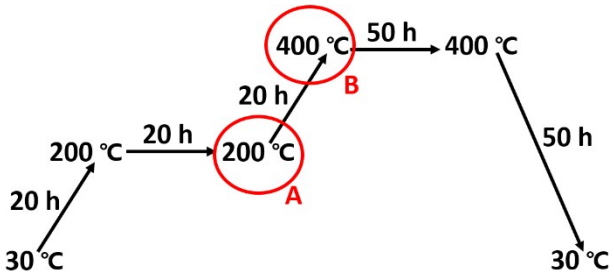

Fig. S5 Synthesis process of the FeSe@FeS material within five steps.

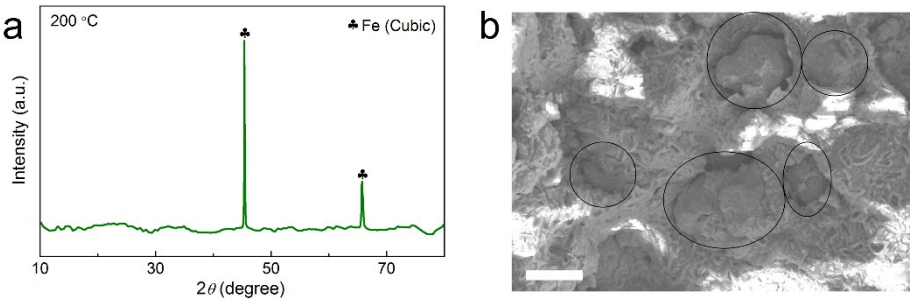

Fig. S6 (a) XRD pattern of the intermediate A in Fig. S5. (b) SEM image of the intermediate A in Fig. S5. The scale bar is 20 μm in panel (b).

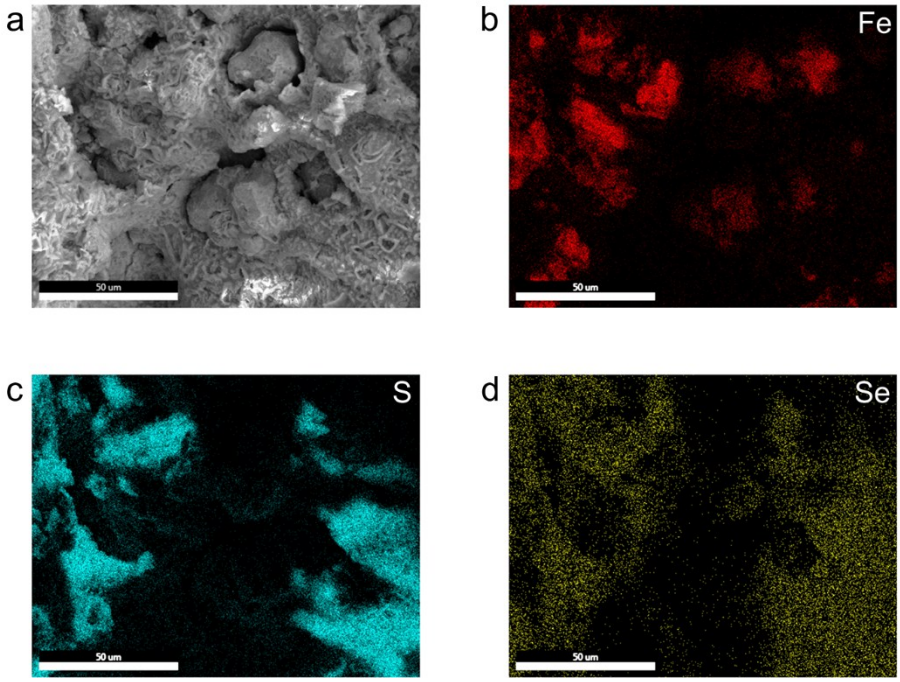

Fig. S7 EDX images of the intermediate A in Fig. S5.

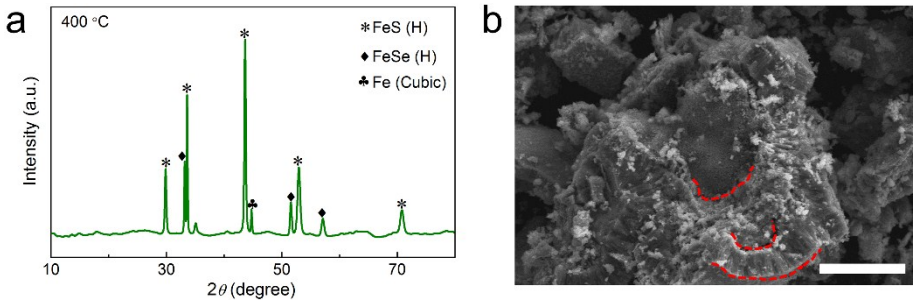

Fig. S8 (a) XRD pattern of the intermediate B in Fig. S5. (b) SEM image of the intermediate B in Fig. S5. The scale bar is 15 μm in panel (b).

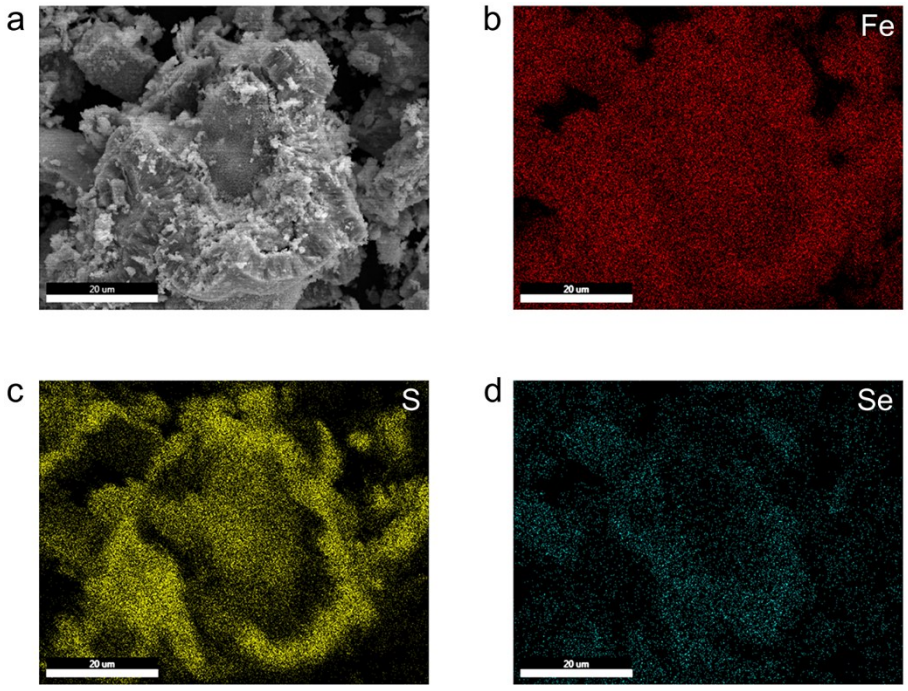

Fig. S9 EDX images of the intermediate B in Fig. S5.

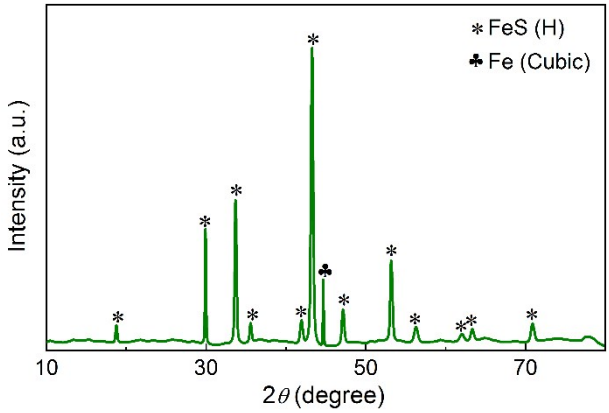

Fig. 10 XRD pattern of the Fe@FeS product without the introduction of raw Se powders (the initial feeding molar ratio between Fe and S elements is 1 : 0.75).

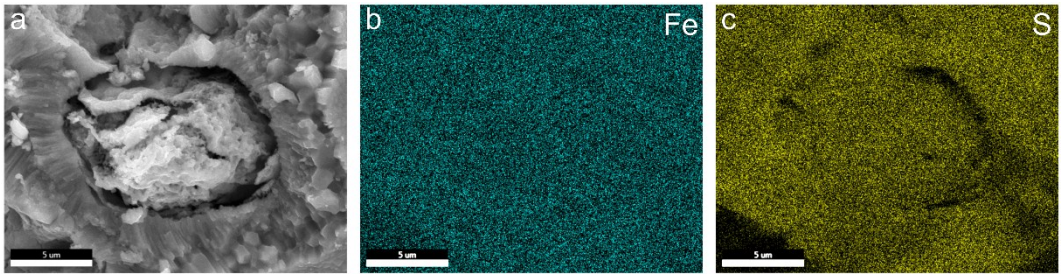

Fig. 11 SEM and EDX images of the Fe@FeS product without the introduction of raw Se powders (the initial feeding molar ratio between Fe and S elements is 1 : 0.75).

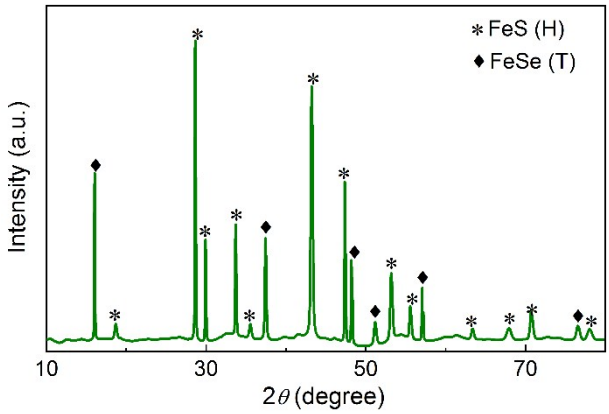

Fig. 12 XRD pattern of the FeSe/FeS product synthesized by the Fe@FeS product and Se powders (the initial feeding molar ratio between Fe element in the Fe@FeS species and added Se element is 1 : 0.25).

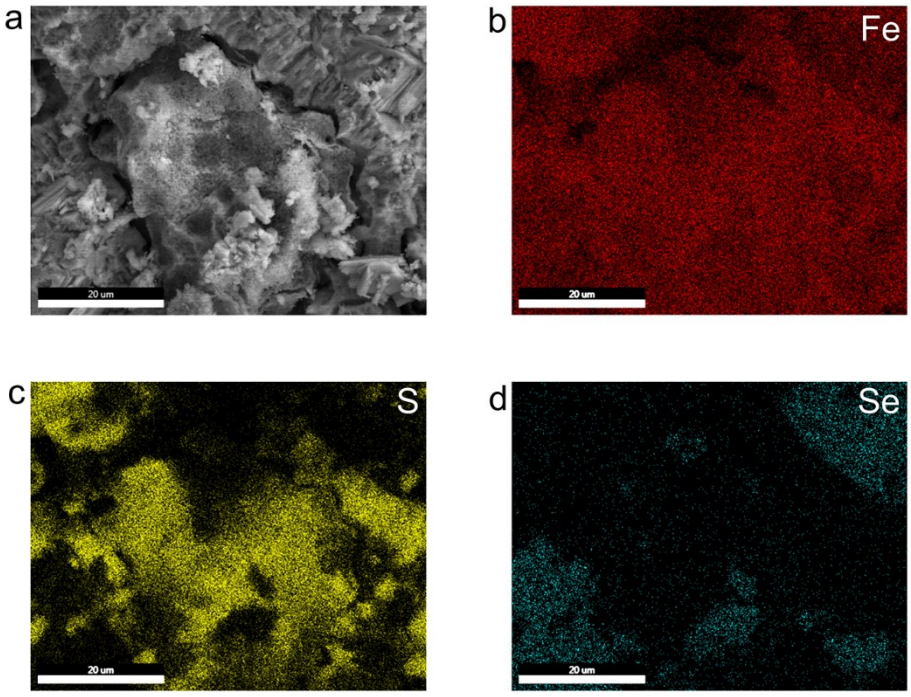

Fig. 13 SEM and EDX images of the FeSe/FeS product synthesized by the Fe@FeS product and Se powders (the initial feeding molar ratio between Fe element in the Fe@FeS species and added Se element is 1 : 0.25).

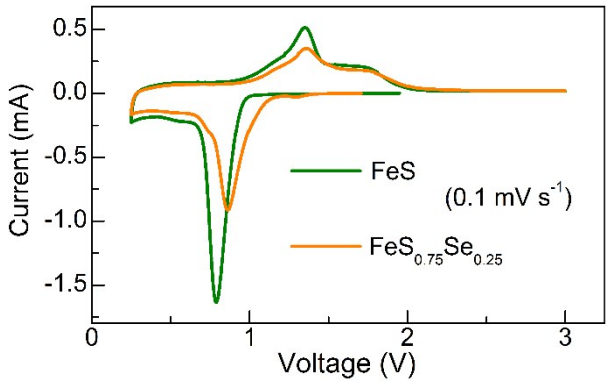

Fig. S14 CV curves of the first sodiation and desodiation processes for the FeSe@FeS and FeS electrodes. The voltage hysteresis of the FeSe@FeS electrode is smaller than that of the FeS electrode.

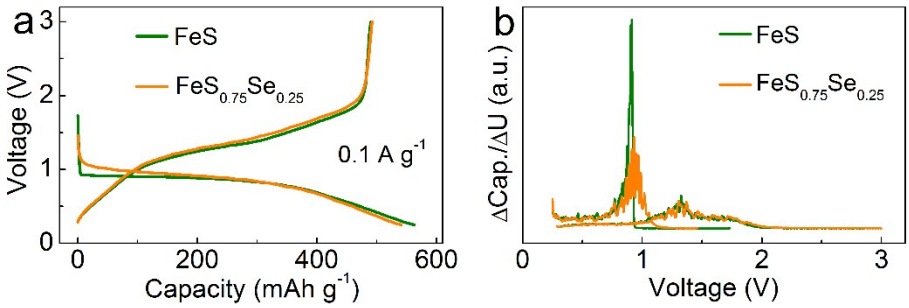

Fig. S15 (a) Galvanostatic discharge-charge curves of the first sodiation and desodiation processes for the FeSe@FeS and FeS electrodes. (b) Change rates of the discharge capacity and charge capacity along with voltage for the FeSe@FeS and FeS electrodes.

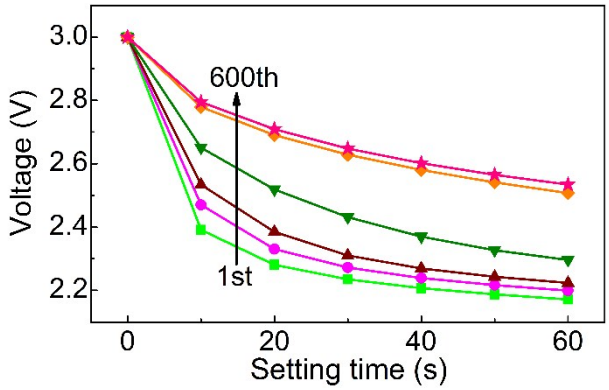

Fig. S16 Voltage drops of the FeSe@FeS electrode during the setting time. For the node of 60 s, the minimum of the voltage drops is 0.466 V for the 600th cycle.

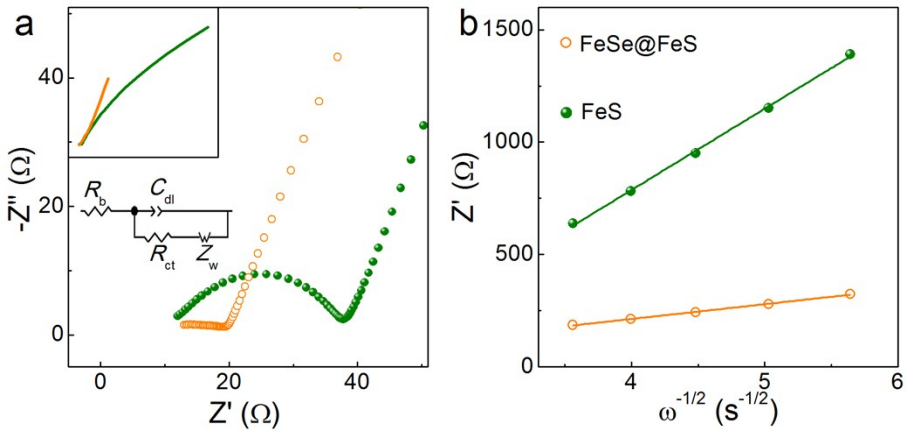

Fig. S17 (a) EIS patterns of the charged-state FeSe@FeS and FeS electrodes. The inset shows the whole patterns. The simulated values of R_{ct} for the FeSe@FeS and FeS electrodes are severally 20 and 28 Ω. (b) Linear relationship of Z_{re} and $\omega^{-1/2}$ in the low-frequency region. The fitted σ (Warburg factor) values for the FeSe@FeS and FeS electrodes are separately 66 and 361.

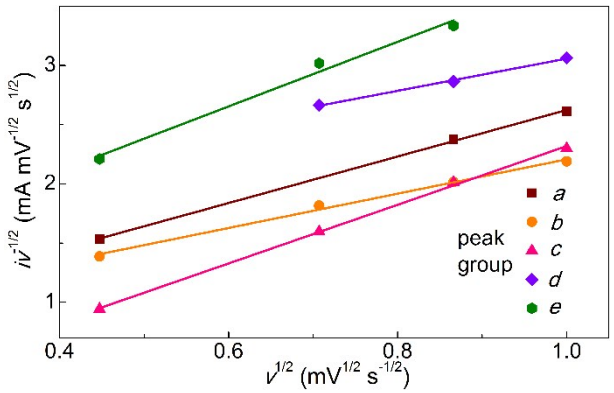

Fig. S18 Dependence of peak current on the scan rate for the peak groups *a*-*e* in Fig. 3b. The slopes and intercepts could be used to simulate the contribution of the pseudocapacitive behavior.

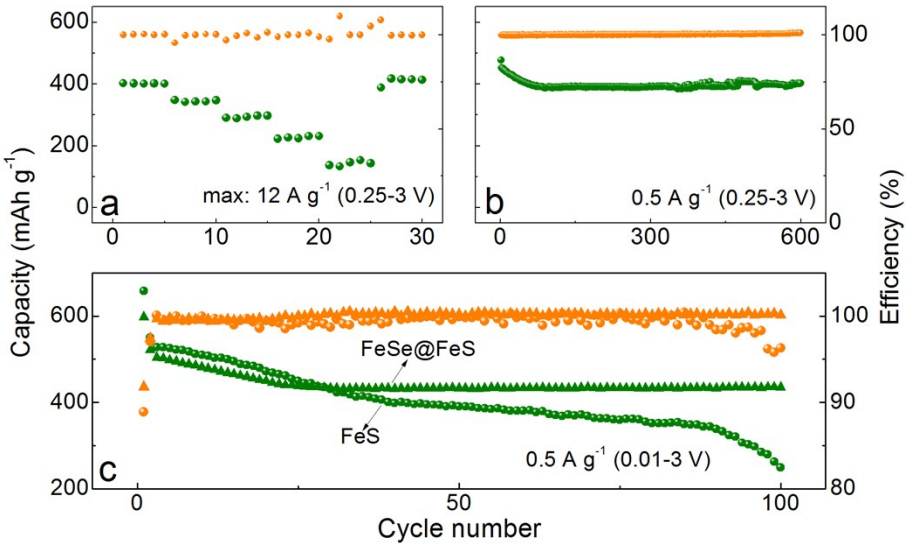

Fig. S19 (a) Rate capability of the FeS electrodes. A low discharge capacity of 143 mAh g^{-1} is delivered at 12 A g^{-1} for the FeS electrodes. (b) Cycling performance of the FeS electrodes performed at 0.5 A g^{-1}. A discharge capacity of 402 mAh g^{-1} is achieved after 600 cycles. (c) Comparison of the cycling performance within the voltage range of 0.01 and 3.0 V between the FeSe@FeS and FeS electrodes. The FeSe@FeS electrodes exhibit better cycling stability than that of the FeS electrodes.

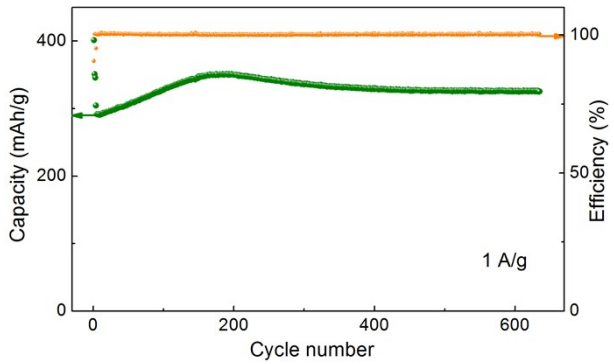

Fig. S20 Cycling performance of the FeSe material at 1 A g^{-1}.

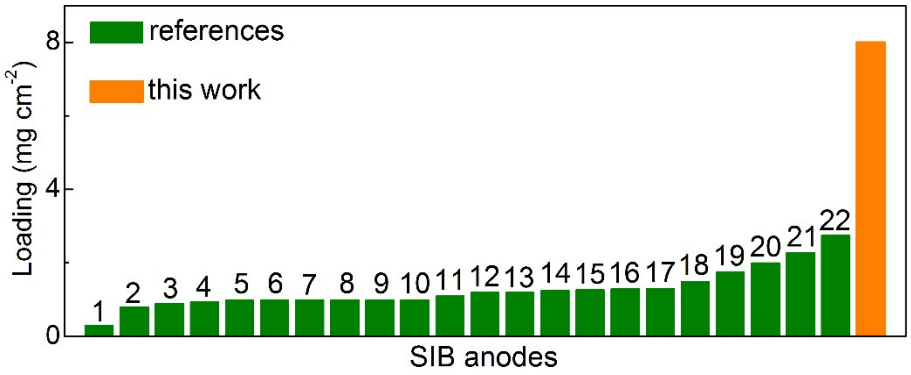

Fig. S21 Comparison of the loadings between the high mass-loaded FeSe@FeS electrodes (8 mg cm^{-2}) and some long-life (over 500 cycles) SIB anodes. References 1-22 severally represents the SnO_2@C-I, G-NCs, NOC, red P-SWCNT, BPPG, γ-Fe_2O_3@C, MoS_2-G2, SnS_2 NC/EDA-RGO, CoS@rGO, C@SnS/SnO_2@Gr, GF+V_2O_3/CNTs, 3D MoS_2-graphene, WS_2@GE, Sb@TiO_{2-x}, H-CoS_2, SbNPs@3D-C, $CoSe_2$, Sn NDs@PNC, 8-Sn@C, MFO@C, SnS_2/rGO, and Mo_3Sb_7@C materials.[1-22]

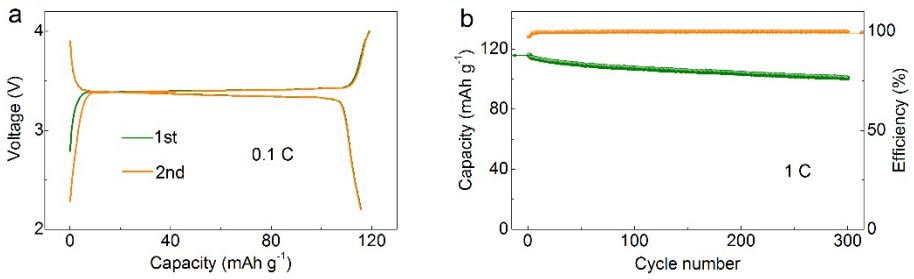

Fig. S22 (a) Galvanostatic voltage profiles of the NVP half cell (with the simulated theoretical capacity of 100 mAh g^{-1}) at 0.1 C between 2.2 and 4.0 V. The initial coulombic efficiency is 97%. (b) Cycling performance of the NVP half cell at 1.0 C between 2.2 and 4.0 V.

Fig. S23 Comparisons of the total exothermic heat (a) and exothermic peak temperature (b) (derived from the DSC data) between the high mass-loaded FeSe@FeS electrodes and some published hard carbons. Letters *a-f* separately represents the HC ($NaClO_4$ in EC + PC), C1600 ($NaPF_6$ in PC), C1600 ($NaPF_6$ in EC + DMC), PBHMC ($NaClO_4$ in EC + PC), C1600 ($NaClO_4$ in PC), C1600 ($NaClO_4$ in EC + DMC) (descriptions in the brackets are the electrolyte systems).[23,24] EC: ethylene carbonate; PC: propylene carbonate; DMC: dimethyl carbonate.

REFERENCES

1 A. Jahel, C. M. Ghimbeu, A. Darwiche, L. Vidal, S. Hajjar-Garreau, C. Vix-Guterl and L. Monconduit, *J. Mater. Chem. A*, 2015, **3**, 11960-11969.

2 D. Li, L. Zhang, H. Chen, J. Wang, L.-X. Ding, S. Wang, P. J. Ashman and H. Wang, *J. Mater. Chem. A*, 2016, **4**, 8630-8635.

3 M. Wang, Z. Yang, W. Li, L. Gu and Y. Yu, *Small*, 2016, **12**, 2559-2566.

4 Y. Zhu, Y. Wen, X. Fan, T. Gao, F. Han, C. Luo, S.-C. Liou and C. Wang, *ACS Nano*, 2015, **9**, 3254-3264.

5 E. M. Lotfabad, J. Ding, K. Cui, A. Kohandehghan, W. P. Kalisvaart, M. Hazelton and D. Mitlin, *ACS Nano*, 2014, **8**, 7115-7129.

6 N. Zhang, X. Han, Y. Liu, X. Hu, Q. Zhao and J. Chen, *Adv. Energy Mater.*, 2015, **5**, 1401123.

7 S. Kalluri, K. H. Seng, Z. Guo, A. Du, K. Konstantinov, H. K. Liu and S. X. Dou, *Sci. Rep.*, 2015, **5**, 11989.

8 Y. Jiang, M. Wei, J. Feng, Y. Ma and S. Xiong, *Energy Environ. Sci.*, 2016, **9**, 1430-1438.

9 S. Peng, X. Han, L. Li, Z. Zhu, F. Cheng, M. Srinivansan, S. Adams and S. Ramakrishna, *Small*, 2016, **12**, 1359-1368.

10 Y. Zheng, T. Zhou, C. Zhang, J. Mao, H. Liu and Z. Guo, *Angew. Chem. Int. Ed.*, 2016, **55**, 3408-3413.

11 X. Xia, D. Chao, Y. Zhang, J. Zhan, Y. Zhong, X. Wang, Y. Wang, Z. X. Shen, J. Tu and H. J. Fan, *Small*, 2016, **12**, 3048-3058.

12 S. H. Choi, Y. N. Ko, J. K. Lee and Y. C. Kang, *Adv. Funct. Mater.*, 2015, **25**, 1780-1788.

13 D. Su, S. Dou and G. Wang, *Chem. Commun.*, 2014, **50**, 4192-4195.

14 N. Wang, Z. Bai, Y. Qian and J. Yang, *Adv. Mater.*, 2016, **28**, 4126-4133.

15 X. Liu, K. Zhang, K. Lei, F. Li, Z. Tao and J. Chen, *Nano Res.*, 2016, **9**, 198-206.

16 W. Luo, P. Zhang, X. Wang, Q. Li, Y. Dong, J. Hua, L. Zhou and L. Mai, *J. Power Sources*, 2016, **304**, 340-345.

17 K. Zhang, M. Park, L. Zhou, G. H. Lee, W. Li, Y. M. Kang and J. Chen, *Adv. Funct. Mater.*, 2016, **26**, 6728-6735.

18 Y. Liu, N. Zhang, L. Jiao and J. Chen, *Adv. Mater.*, 2015, **27**, 6702-6707.

19 Y. Liu, N. Zhang, L. Jiao, Z. Tao and J. Chen, *Adv. Funct. Mater.*, 2015, **25**, 214-220.

20 Y. Liu, N. Zhang, C. Yu, L. Jiao and J. Chen, *Nano Lett.*, 2016, **16**, 3321-3328.

21 Y. Zhang, P. Zhu, L. Huang, J. Xie, S. Zhang, G. Cao and X. Zhao, *Adv. Funct. Mater.*, 2015, **25**, 481-489.

22 W. Li, C. Hu, M. Zhou, H. Tao, K. Wang, S. Cheng and K. Jiang, *J. Power Sources*, 2016, **307**, 173-180.

23 A. Ponrouch, A. Goñi and M. R. Palacín, *Electrochem. Commun.*, 2013, **27**, 85-88.

24 J. Zhao, L. Zhao, K. Chihara, S. Okada, J.-i. Yamaki, S. Matsumoto, S. Kuze and K. Nakane, *J. Power Sources*, 2013, **244**, 752-757.